PCCP

PAPER

View Article Online
View Journal

Cite this: DOI: 10.1039/d5cp04917b

Investigation of zirconium interactions with a DOTA based theranostic hybrid nanoparticle using X-ray absorption spectroscopy

Ilyes Mahti, †[a] Laurence Berthon, [a] Charles Truillet, [b] Bertrand Kuhnast, [b] Thomas Dumas [a] and Dominique Guillaumont *[a]

Chelator-based nanoparticles have gained significant attention for theranostic applications due to their tunable properties and biocompatibility. Among them, AGuIX nanoparticles (NPs) are promising ultrasmall nanoparticles composed of a polysiloxane core surrounded by DOTAGA chelates, derivatives of DOTA (1,4,7,10-tetraazacyclododecane-1,4,7,10-tetraacetic acid), enabling both radiosensitization and medical imaging. ^{89}Zr is a particularly promising radioisotope and its radiolabeling on the AGuIX nanoparticles is highly efficient, whereas Zr–DOTA-complex formation requires heating. Understanding the interaction between radionuclides and nanoparticles is crucial to achieve successful radiolabeling strategies. In this regard, X-ray absorption spectroscopy (XAS) is one of the few experimental techniques capable of providing structural information for such nanoparticles in solution. By combining EXAFS, XANES and theoretical calculations, the coordination chemistry of zirconium in Zr–AGuIX nanoparticles is compared to Zr–DOTA, explaining the high ^{89}Zr labeling yield of AGuIX. In the Zr–DOTA complex, Zr adopts an eight-coordinated structure and is inserted into the DOTA cage. In contrast, in Zr–AGuIX, zirconium is not bound within the DOTAGA cage but instead coordinates with six oxygen atoms at shorter distances from deprotonated silanols groups and carboxylate groups from DOTAGA, increasing its stability. These findings indicate that flexible carboxylate groups could effectively enhance the zirconium radiolabeling efficiency of such silica-based nanoparticles.

Received 17th December 2025,
Accepted 5th May 2026

DOI: 10.1039/d5cp04917b

rsc.li/pccp

I. Introduction

In recent years, nanoparticle development has extended to a wide range of medicinal applications, mainly in cancer diagnosis and treatment. They can be inorganic (silica, iron or gold oxide nanoparticles) or organic (lipids, polymeric micelles, carbon nanotubes). Amongst the various types of nanoparticles, silica nanoparticles have attracted considerable attention for nano-oncology applications. Their appeal is due to their ease of preparation and the possibility of controlling their size, porosity and shape. Furthermore, they are biocompatible and very low in toxicity, which makes their use in oncology highly attractive. They can also be designed to incorporate different imaging and therapeutic agents into their pores or on their surface. Their surface can be easily functionalized, and organic ligands can be grafted onto them to add or enhance properties of interest in oncology. Recent works on the application of nanomaterials in nuclear medicine are particularly interested in hybrid (organic and inorganic) nanoparticles (NPs) with the use of medical metal radionuclides (radiometals) such as ^{89}Zr, ^{111}In, ^{64}Cu or ^{68}Ga.[1–10] Radiometals possess the most suitable properties for single photon emission computed tomography (SPECT) and positron emission tomography (PET) applications. The strength of radiolabeled nanoparticles is that different imaging and therapy techniques can be integrated into a single nanoparticle to obtain synergetic advantages.[11,12] For example, the bimodal PET-MRI system incorporates the high sensitivity of PET with the high resolution of MRI.[13] In this type of system, the presence of a stable chelating agent is crucial to prevent the radiometal release.

The novel radiosensitizing AGuIX (Activation and Guidance of Irradiation by X-ray) are particularly promising ultrasmall NPs.[14,15] Currently, they are one of the few silica-based nanoparticles which have been approved for clinical use and recent literature has shown how AGuIX NPs can be used to perform image-guided radiation therapy and to enhance radiotherapy efficacy (radioenhancer).[14–18] Their synthesis goes under a top

[a] CEA, DES, ISEC, DMRC, Univ Montpellier, Marcoule, France. E-mail: dominique.guillaumont@cea.fr
[b] Laboratoire d'Imagerie Biomédicale Multimodale Paris Saclay CEA, INSERM, CNRS, Université Paris-Saclay, Orsay 91401, France
† Current affiliation: Chalmers University of Technology, Department of Chemistry and Chemical Engineering, Nuclear Chemistry and Industrial Materials Recycling, Gothenburg, SE-412 96, Sweden.

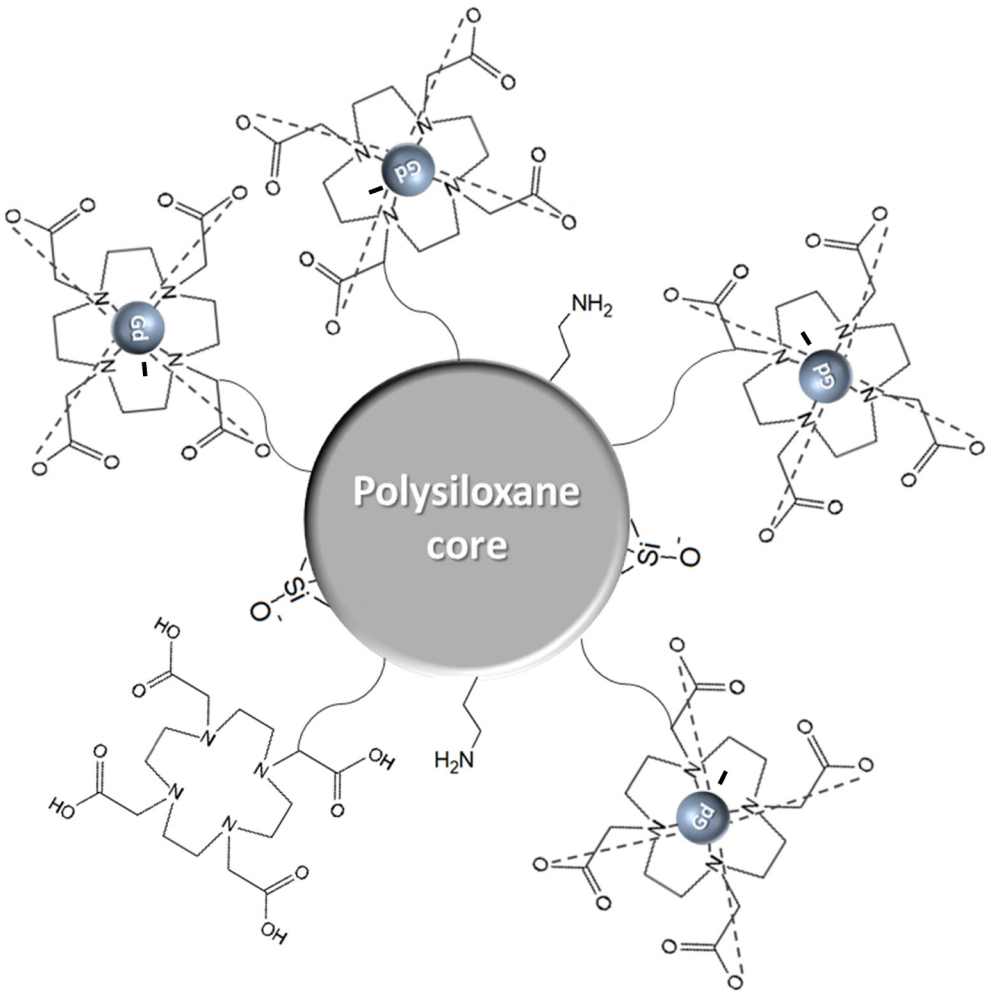

Fig. 1 Schematic representation of AGuIX nanoparticle.

down process well described by Mignot *et al.*[19] A polysiloxane shell is grown around gadolinium oxide cores using hydrolysis-condensation of (3-aminopropyl)triethoxysilane (APTES) and tetraethoxysilane (TEOS). DOTAGA ligands (5-(2-aminoethylamino)-5-oxo-2-[4,7,10-tris(carboxymethyl)-1,4,7,10-tetrazacyclododec-1-yl] pentanoic acid) are then grafted onto the surface. The DOTAGA ligand is similar to the well-known DOTA (1,4,7,10-tetraazacyclododecane-1,4,7,10-tetraacetic acid) ligand but includes an additional arm with an amide functional group. This extra arm enables the ligand to be attached to the nanoparticle through peptide coupling. Finally, the resulting compound is transferred to water, where the gadolinium oxide core dissolves, and Gd^{3+} ions are chelated by some of the DOTAGA ligands. This transfer to water results in ultrasmall nanoparticles (mean hydrodynamic parameter < 5 nm) with a polysiloxane core with two types of DOTAGA attached to the surface: Gd-DOTAGA complexes and "free" DOTAGA (Fig. 1). The presence of these complexes allows the NP to be used as a contrast agent in MRI and to improve the effectiveness of radiotherapy (radiosensitizing effect).

In addition, primary amines ($-NH_2$) derived from APTES are present and can be used to attach additional chelators such as DFO (deferoxamine) through peptide coupling.[2] Silanol groups (–Si–OH), which can be deprotonated ($-Si-O^-$) at pH values above 2–3,[6,20,21] are also found on the surface. The freely accessible DOTAGA (or additional chelators) can bind radionuclides, allowing the combination of multiple techniques. Amongst the radioisotopes, zirconium-89 is particularly promising as a positron emitter with a long half-life period to be used in PET imaging. However, one difficulty is to bind the radiometal inside the DOTAGA cavity within the tetraaza core. This can be especially difficult for highly hydrated Zr(IV) ion. The formation of Zr(IV)–DOTA complex has been reported in the literature,[22,23] but in aqueous media, the reaction requires heating at 90 °C for 45 min to form the ^{89}Zr–DOTA complex.[22] Without heating, the Zr–DOTA complex can still form, but with a significantly lower yield.[24] However, Tran *et al.* demonstrated that AGuIX NPs can be directly labeled with ^{89}Zr, thanks to the accessible DOTAGA moieties, with an unexpectedly high labelling yield ($96.5 \pm 1.5\%$).[1] The authors initially supposed that Zr was chelated by the accessible DOTAGA ligands to form the Zr–DOTAGA complex. It was assumed that Zr(IV) is encapsulated within the DOTAGA cavity but no information was available on the coordination sphere of Zr in AGuIX NPs to confirm this hypothesis. They hypothesized that silanol

groups (Si–OH and Si–O^-) and primary amines (–NH_2) on the nanoparticle's surface could facilitate the complexation of Zr inside DOTAGA of the nanoparticle. Chen *et al.* showed that Zr can bind to silica nanoparticles even without surface-grafted ligands but that complexation with silanols in unfunctionalized nanoparticles is weaker than in AGuIX.[1,6] Indeed, AGuIX radiolabeling with Zr is more efficient; at 37 °C after one hour and at pH = 7–8. 96% of Zr is bound to the nanoparticle, whereas only 27% of Zr is bound to the unfunctionalized nanoparticle.[5,6] In the case of silica nanoparticles with DFO ligands grafted to their surface, a Zr radiolabeling yield four times higher was observed compared to unfunctionalized nanoparticle.[5] Moreover, ^{89}Zr release was detected in bones with the ligand-free nanoparticle in *in vivo* tests on mice.[6] These results indicate that the ligand (DOTA or DFO) plays a role in the labeling of Zr on the nanoparticle. Understanding how ^{89}Zr can be complexed within a DOTA–polysiloxane structure is crucial for theranostic applications, particularly with therapeutic radiometals such as lutetium-177 (^{177}Lu), where DOTA is commonly used as a chelator. Employing the same chelate structure for both ^{89}Zr and ^{177}Lu would enable visualization of the complete kinetic biodistribution of the radioligand using PET imaging (^{89}Zr) prior to administering the therapeutic radiopharmaceutical with ^{177}Lu.

For these promising new nanoparticles labeled with radionuclides, it is particularly challenging to characterize the nanoparticle–radiometal interaction and to determine the role of the different chemical groups present of the surface. X-ray absorption spectroscopy (XAS) is one of the few experimental techniques, which can provide structural information for such nanoparticles in solution. Specifically, extended X-ray absorption fine structure (EXAFS) and X-ray absorption near-edge structure (XANES) can unravel the coordination geometry of metal ions at the particle surface. In the present work, we have used EXAFS and XANES to characterize the interaction between zirconium and AGuIX nanoparticles. Theoretical calculations were also employed to extract better information from the experimental spectra. Our first objective was to identify the chemical groups involved in the Zr coordination sphere. We began by investigating Zr–DOTA complex in solution as a reference system. Here, we sought to specifically obtain reference EXAFS and XANES data for encapsulated Zr in DOTA. Using these reference data, we further examined Zr coordination structure in AGuIX nanoparticles. DFT and *ab initio* multiple scattering calculations were performed to complement the XAS results.[25–27]

II. Materials and methods

Chemicals

DOTA in solid form was purchased from Chematech (Dijon, France) with a confirmed purity exceeding 98% as verified by HPLC. Solid zirconium(IV) acetylacetonate was obtained from Sigma-Aldrich with a purity of 97%. Anhydride methanol from Sigma-Aldrich (purity 99.8%) was employed. A biological buffer was used: HEPES (4-(2-hydroxyethyl)-1-piperazine ethane sulfonic acid, $C_8H_{18}N_2O_4S$, Sigma-Aldrich, purity ≥ 99.5%). Finally, the AGuIX nanoparticle was supplied by Service Hospitalier Frédéric Joliot (CEA, Dr Charles Truillet). Regular AGuIX are composed of DOTA ligand, and 97–99% of which are complexed with Gd^{3+} ions. This has been demonstrated using Cu^{2+} and Eu^{3+} titration method.[19,28,29] In this work, we worked with AGuIX@DOTA2%. It contains 2% of free DOTA used for zirconium complexation, the rest being bound to gadolinium cations. All commercial products were used as received without further purification. It is important to note that in this work all the chemicals used are non-radioactive. Zr always refers to natural Zr whereas ^{89}Zr refers to the actual radioisotope species (used in the literature as an element or complex with a chelate).

Synthesis and characterization of Zr–DOTA and Zr–DOTAGA

Synthesis of Zr–DOTA has been performed according to a previous work.[24] The presence of the complex has been confirmed by NMR and ESI-MS experiments. Zr–DOTAGA has also been synthesized according to the same protocol by replacing DOTA ligand by NH_2–DOTAGA. The presence of the complex has been confirmed by ESI-MS (m/z = 605).

Sample preparation

Four samples were prepared for the XAS analysis, their compositions are given in Table 1. The detection limit of the XAS instrument is approximatively 10^{-4} mol L^{-1}. Consequently, the radiolabeling protocol of AGuIX with ^{89}Zr described in the literature for ^{89}Zr concentration about 1.2×10^{-7} mol L^{-1} was adapted to increase the zirconium concentration.[1]

The modified protocol is as follows: to a solution of $Zr(AcAc)_4$ in water, an excess of carbonates (7×10^{-2} mol L^{-1} of Na_2CO_3) is added. HEPES solution in water (0.5 mol L^{-1}) is then added to adjust the pH to approximately 7 (sample Zr–A in Table 1). HEPES is a biological buffer that does not complex metals, thus preventing cation-nanoparticle interactions.[30] Next, the AGuIX nanoparticle, dissolved in a 0.5 mol L^{-1} HEPES solution in water, is added to the Zr solution. The mixture is then shaked and heated at 37 °C for 1 h (sample Zr–AGuIX in Table 1).

Two additional samples were prepared with DOTA ligand instead of AGuIX nanoparticles. The Zr–DOTA sample was prepared following the protocol previously described.[24] It corresponds to Zr–DOTA complex in aqueous solution (sample Zr–DOTA in Table 1). A last sample was prepared using the same

Table 1 Compositions of the samples, concentrations are in mol L^{-1}

	Zr–DOTA	Zr–AGuIX	Zr–A	Zr–B
[DOTA]	5×10^{-3}	1.4×10^{-3} [a]	—	4.2×10^{-3}
[AGuIX]	—	7×10^{-2}	—	—
[Zr]	5×10^{-3}	7×10^{-4}	7×10^{-4}	7×10^{-4}
[Na_2CO_3]	—	7×10^{-2}	7×10^{-2}	7×10^{-2}
[HEPES]	—	4.3×10^{-1}	4.3×10^{-1}	4.3×10^{-1}
pH	5.7	7	7.2	7

[a] The [DOTA] in the Zr–AGuIX sample is evaluated considering that free DOTA accounts for 2% of the total AGuIX content.

protocol as for Zr–AGuIX but replacing AGuIX by a DOTA ligand (Zr–B sample in Table 1).

The comparison between samples Zr–A (Zr in HEPES and carbonate medium) and Zr–AGuIX aims to confirm whether the nanoparticle influences the coordination mode of Zr. Additionally, comparing Zr–B sample with Zr–DOTA and Zr–AGuIX samples will help determine whether zirconium enters the DOTA ligand cage under these conditions (comparison of Zr–B and Zr–DOTA) and to check if DOTA in solution and accessible DOTAGA moieties grafted onto the nanoparticle exhibit the same behavior (comparison of Zr–B and Zr–AGuIX).

X-ray absorption data acquisition and treatment

The samples were analyzed on the MARS beamline (2.75 GeV at 450 mA) at the SOLEIL synchrotron (Saint-Aubin, France). The beamline is equipped with a double Si(220) crystal monochromator (DCM). Two Pt-coated mirrors, placed before and after the DCM, were employed to reject higher-order harmonics and to achieve collimation and focusing of the beam. A metallic zirconium foil was regularly used for energy calibration. A 13-element HPGe solid-state detector was used for data collection in fluorescence mode. All measurements were performed at room temperature in 200 mL double-layered cells. Three to four spectra per sample were recorded at the Zr K edge (17 998 eV), then normalized and merged using the ATHENA software.[31] After energy calibration, the E_0 energy was set at the maximum of the derivative of the absorption. Fourier transforms (FTs) were performed on the k^3-weighted EXAFS spectra between 2.5 and 12 $Å^{-1}$. All fitting operations were performed in R-space between 1 and 3 or 6 Å using ARTEMIS software with the IFEFFIT code.[31] The amplitude factor ${S_0}^2$ was set at 1.05, in line with previous work on X-ray absorption spectroscopy studies of zirconium-based compounds.[32] Back-scattering amplitude and phase-shift functions were obtained from FEFF 8.4 calculations.[31] The R-factor (%) is provided by the ARTHEMIS software.

Computational details

All calculations were conducted using density functional theory (DFT) with Gaussian 16.[33] The PBE0 functional was employed.[34] The optimized geometries were verified as true minima through frequency calculations, as no imaginary frequencies were detected. The 6-31G+(d,p) basis set was used for H, C, N, and O atoms. For zirconium, core electrons were represented by the MWB28 Stuttgart-Cologne quasi-relativistic effective core potential (ECP), along with the corresponding basis set for valence electrons.[35] Water was modeled using the self-consistent reaction field (SCRF) method with the polarizable continuum model (IEFPCM).[36]

The XANES and EXAFS calculations were done using FEFF 9.05 code using the real-space Green's function approach. For the EXAFS calculations, all multiple-scattering paths were calculated up to an R-path of 6 Å. The Debye–Waller factors for each scattering path were calculated from the DFT calculations of vibrational frequencies with Gaussian 16 and using the DMDW module included in FEFF (at 300 K).[37]

III. Results and discussion

Zr–DOTA complexes

The synthesis and characterization of Zr–DOTA complexes have been well described in solution from NMR spectroscopy and in the solid state from crystal structure determination using single crystal X-ray diffraction analysis.[22,24] The chelation by the four macrocycle nitrogen atoms and four oxygen atoms of the pendant arms was demonstrated in solution by NMR spectroscopy. Here, we want to obtain EXAFS spectra for the Zr–DOTA complexes in aqueous solution, which have not been reported so far in order to further confirm the chelation and to obtain EXAFS reference data. For lanthanides(III) and actinides(III), two coordination structures have been found in solution. The first one corresponds to an out-of-cage complexation (C1) with the chelation by four oxygen atoms of the pendant arms of DOTA and by water molecules. The second structure (C2) corresponds to the chelation by the four macrocycle nitrogen atoms and four oxygen atoms of the pendant arms.[38] The out-of-cage complexation (C1) has been observed with lanthanides(III)–DOTA and actinide(III)–DOTA as an intermediate complex in solution, which is formed before the final C2 complex.[39–41] The presence of these complexes for lanthanides has been confirmed by EXAFS experiments.[39]

Prior to the EXAFS experiments, theoretical calculations were conducted for these two coordination environments for Zr in order to simulate the EXAFS spectra and to determine whether there is a difference between the spectra of the two structural models. The geometries of the two C1 and C2 structural models were first optimized from DFT calculations for (i) Zr bonded only to the carboxylic functions and 4 water molecules that complete its coordination sphere, $[Zr(DOTA)(H_2O)_4]$ (C1-type complex) (ii) Zr "encapsulated" into the macrocyclic cage, bonded to the carboxylic functions and tetraaza nitrogen atoms, Zr–DOTA (C2-type complex).

The EXAFS spectra were simulated; Debye–Waller factors and atomic positions were obtained from the DFT calculations using vibrational frequencies and geometry optimized structures. The structural parameters of the DFT-optimized geometries are given in supporting information. The results are reported in Fig. 2. A comparison of the EXAFS oscillation signal reveals a significant difference. Specifically, a signal splitting between 4 and 5 $Å^{-1}$ is observed only for Zr–DOTA. This splitting is due to the presence of two diffusion paths of different lengths within the first coordination sphere of Zr; Zr–O and Zr–N (2.14 and 2.49 Å respectively). Therefore, the signal splitting around 4–5 $Å^{-1}$ serves as a reliable indicator of zirconium encapsulation within the DOTA cage.

The EXAFS spectrum of the Zr–DOTA complex was recorded at the zirconium K-edge (E_0 = 17998 eV). The k^3-weighted EXAFS spectrum and its corresponding Fourier transform (FT) are shown in Fig. 3. The signal splitting between 4 and 5 $Å^{-1}$, characteristic of encapsulation according to the previous simulations, is observed, indicating the formation of the final C2 complex. This signal splitting is reflected on the FT by a broadening and shouldering of the main contribution (1 Å < R-φ < 2 Å), indicating the presence of two types of bonds in the first coordination sphere, Zr–O and Zr–N. The contributions of

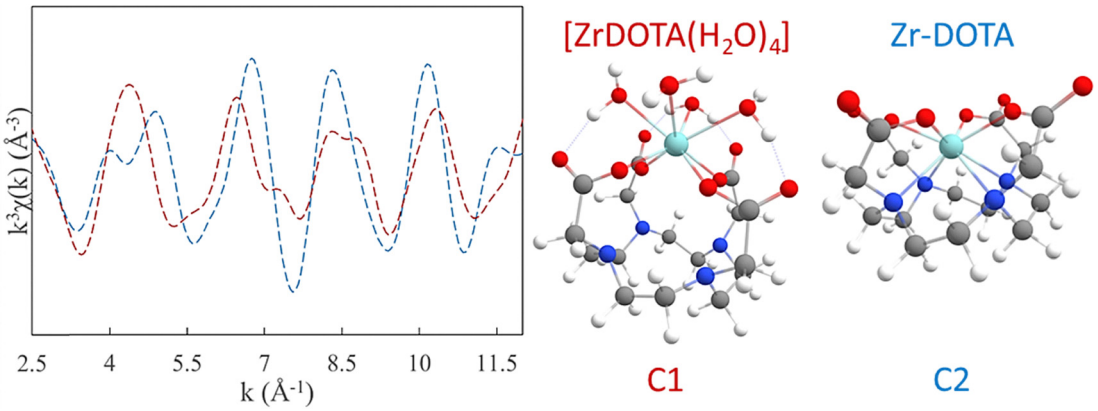

Fig. 2 Simulated EXAFS signal for the DFT-optimized structures [Zr(DOTA)(H_2O)$_4$] (C1-type complex) (red) and Zr–DOTA (C2-type complex) (blue). Carbon atoms are shown in gray, oxygen in red, nitrogen in blue, hydrogen in white and zirconium in light blue.

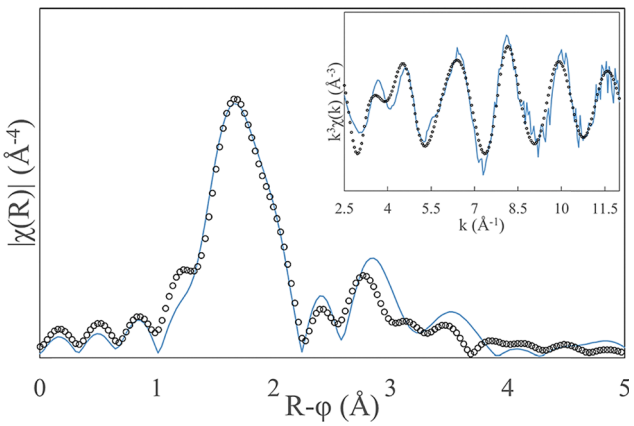

Fig. 3 Fourier transform of the Zr K edge k^3-weighted EXAFS spectrum ($2.5 \leq k \leq 12$ Å^{-1}) of Zr–DOTA in water, experimental data (blue line) and best fit results (empty black circle). [Zr–DOTA] = 5×10^{-3} mol L^{-1}, pH = 6.

the carbon atoms are observed between R-φ = 2.2 Å and 3.8 Å. Zirconium is therefore well encapsulated within the DOTA cage. This finding is in agreement with ^{1}H NMR spectra previously reported.[24]

The possible presence of Zr clusters in solution was then investigated as Zr(IV) ions are easily hydrolyzed and polymerize to form polynuclear species. Hennig *et al.* isolated the tetranuclear hydrolyzed zirconium species, $[Zr_4(OH)_8(OH_2)_{16}]^{8+}$, as well as a hexanuclear zirconium cluster surrounded by acetate, $Zr_6(O)_4(OH)_4(CH_3COO)_{12}$.[42] The EXAFS spectra were reported for these species. On the Fourier transform, both species show a Zr–O–Zr contribution at R-φ = 3.2 Å with high intensity and another at 4.7 Å with low intensity. No contribution at these R-φ values is observed in the Fourier transform of the Zr–DOTA sample, indicating that, if these species exist, they are present in very low quantities. Furthermore, as demonstrated in a similar study with Pu(IV), the metal must be outside the DOTA cage to form clusters (due to steric constraint).[43] Therefore, the presence of Zr clusters can been ruled out.

Finally, the experimental EXAFS spectrum of the Zr–DOTA complex was fitted using the crystallographic structure from the study by Pandya *et al.*[22] For the fit, 48 diffusion paths were considered. Coordination numbers were fixed at four oxygens and four nitrogen atoms to be consistent with crystallographic data.

The best-fit results are in correct agreement with the experimental data for Zr–DOTA as shown in Fig. 3. The best-fit parameters are provided in Table 2. According to the XRD crystal structure, the first coordination sphere can be split into two groups of degenerated diffusion paths. The first paths correspond to the four oxygen atoms, at a fitted distance of 2.17 Å. The second path, at a longer distance, corresponds to the four nitrogen atoms at a fitted distance of 2.51 Å. The longer distances obtained from the fit compared to the XRD model may result from differences between the solid state and the solution. The high Debye–Waller factor obtained for Zr–N (0.012 Å^2) may be due to the presence of additional minor species in solution (conformers, hydrolyzed species, *etc.*). This disordered Zr–N bonds also translate in the bond length that differs from the XRD crystal structure by 0.1 Å.

Table 2 EXAFS best fit parameters for Zr–DOTA

Scattering path	Best-fit parameters for Zr–DOTA (S_0^2 = 1.05, ΔE_0 = 2.7 ± 2, *R*-factor = 11%)			Zr–DOTA from XRD[22]	
	N	σ^2 (Å^2)	*R* (Å)	*N*	*R* (Å)
Zr–O	4	0.004(1)	2.17(1)	4	2.133
Zr–N	4	0.012(5)	2.51(4)	4	2.415
Zr–C	4	0.016(5)	3.09(5)	4	3.039

Amplitude reduction factor S_0^2 and coordination number *N* were fixed. ΔE_0: threshold energy shift in eV; σ^2: Debye-Waller factor; *R*: interatomic distance. Uncertainties of the last digit are given in brackets.

Zr–AGuIX

The experimental EXAFS spectra of the Zr–DOTA complex and Zr–AGuIX sample are compared on Fig. 4. The spectra show significant differences, indicating a variation in the zirconium coordination sphere between the two compounds. The primary difference between the spectra is observed at 4 Å^{-1}, where a

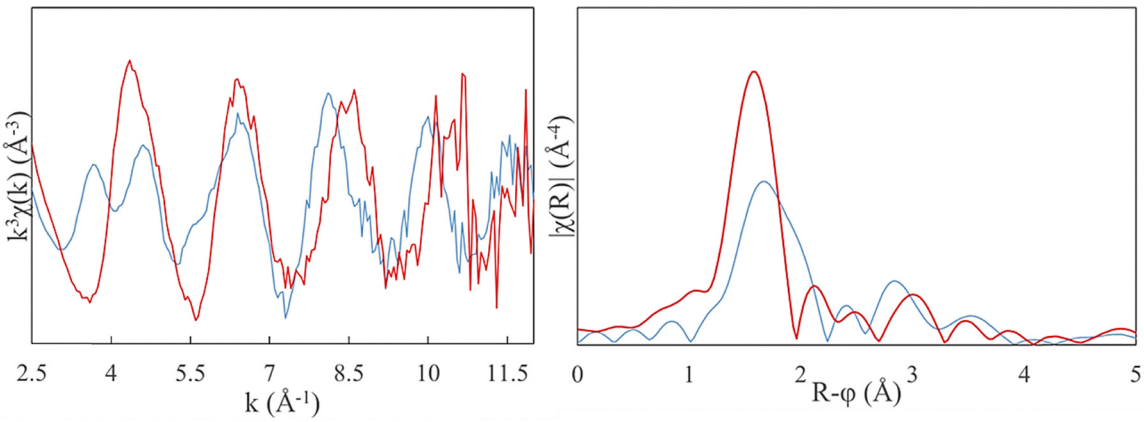

Fig. 4 Zr K-edge EXAFS spectra (left) and its Fourier transform (right) of Zr–DOTA (blue) and Zr–AGuIX (red).

signal splitting appears only for Zr–DOTA. This signal splitting, as described in the first part, is due to the presence of atoms at multiple distances in the first coordination sphere and indicates that zirconium is located within the DOTA cage. It is reflected in the Fourier transform by a broadening and shouldering of the first peak (Fig. 4). The broadening of this peak suggests a large distribution of distances in the first coordination sphere, likely corresponding to the presence of both short (Zr–O) and long (Zr–N) bonds. In the case of Zr–AGuIX sample, the peak is thinner and more intense. This indicates the presence of only one oxygen shell in the first coordination sphere, that appears to be at a shorter distance than the broad peak of Zr–DOTA on the Fourier Transform, and the absence of nitrogen atoms at longer distances. Additionally, the frequency of EXAFS oscillations is lower for the Zr–AGuIX sample compared to the Zr–DOTA complex, confirming the presence of shorter bonds in Zr–AGuIX.

In conclusion, for Zr–DOTA complex, zirconium is inside the DOTA cage, bonded to the four oxygen atoms of the carboxylate arms and the four nitrogen atoms of the cyclene (C2 complex). In contrast, for Zr–AGuIX sample, zirconium is not bonded to the four nitrogen atoms (it is not inside the DOTAGA cage) and is only bonded to oxygen atoms at shorter distances. In addition, it seems that no polynuclear Zr cluster is formed in the Zr–AGuIX sample, given the absence of Zr–O–Zr contribution on the Fourier transform (Fig. 4).

To determine whether the nanoparticle is involved in Zr coordination, the EXAFS spectrum of Zr–AGuIX sample is compared with two other experimental spectra (Fig. 5), recorded for Zr–A sample (Zr in aqueous solution in the presence of Na_2CO_3 and HEPES, pH = 7.2) and for Zr–B sample (Zr in solution in the presence of Na_2CO_3, HEPES and DOTA, pH = 7) (see Table 1). Here, the aim is to compare the coordination sphere of Zr in the presence and absence of DOTA or AGuIX in solution to determine whether the structural change for Zr–AGuIX originates from the synthesis medium or from the presence of the nanoparticle. First, the signal splitting at 4 $Å^{-1}$ is not observed for Zr–B sample indicating that zirconium is not inside the DOTA cage. This is consistent with the known difficulty of forming the Zr–DOTA complex in aqueous phase without heating.[1] In addition to the partial hydrolysis of zirconium in the aqueous phase that can occur at pH = 7, carbonate ions may favor the formation of zirconium carbonate complexes over DOTA complexation ($pK_a(CO_2/HCO_3^-)$ = 6.35, $pK_a(HCO_3^-/CO_3^{2-})$ = 10.33). Moreover, the spectra of Zr–B and Zr–A samples are very similar, suggesting that the environment around Zr is the same in these two samples. However, it is important to highlight that the EXAFS spectrum of Zr–AGuIX sample differs considerably from those of

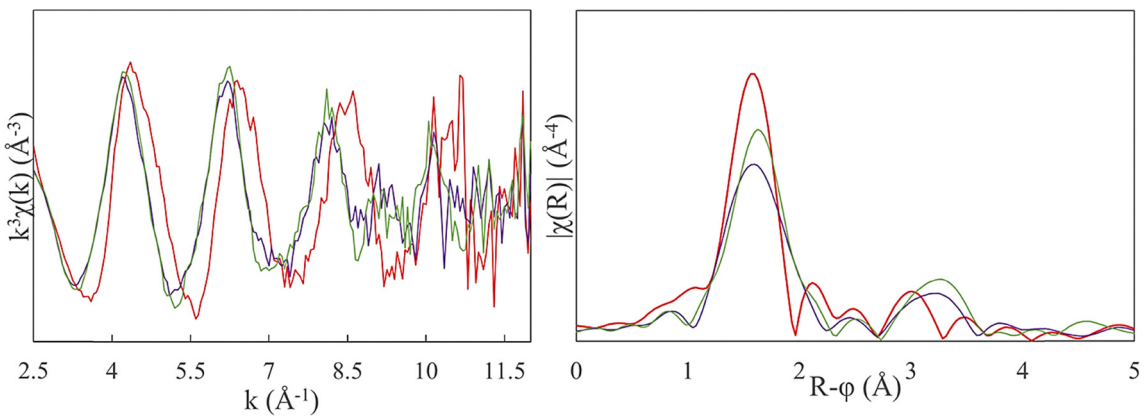

Fig. 5 Zr K-edge EXAFS spectra (left) and its Fourier transform (right) of Zr–A (green line), Zr–B (purple line) and Zr–AGuIX (red line).

Table 3 Best-fit parameters for the Zr K-edge EXAFS spectra of Zr–A and Zr–AGuIX using a one-shell model. Fitting was performed for k ranging from 2.5 to 12 Å^{-1} and over the 1–3 Å range

	Fitting parameters[a]				
Sample	ΔE_0	N	σ^2 (Å^2)	R (Å)	R-factor (%)
Zr–A	0(2)	7.0(13)	0.010(2)	2.19(2)	6
Zr–AGuIX	−3(2)	5.1(8)	0.005(1)	2.10(1)	4

[a] Amplitude reduction factor $S_0{}^2$ set at 1.05. ΔE_0: threshold energy shift; N: coordination number; σ^2: Debye–Waller factor; R: interatomic distance. Uncertainties of the last digit are shown in brackets.

Zr–A and Zr–B samples. This indicates that the addition of the AGuIX nanoparticles in a solution of Zr in buffered aqueous media changes the coordination sphere of zirconium.

These results indicate that zirconium bound to AGuIX is not present inside the DOTA cage (it is not bound to the 4 nitrogen atoms) and that the nanoparticle plays a role in zirconium complexation.

To further analyze the EXAFS spectra, a fit was performed for Zr–AGuIX and Zr–A using a simple one-shell model of oxygen atoms located at an equal distance from Zr. A fit was also performed using Zr–DOTA from Pandya *et al.* study but was not conclusive.[22] The number of oxygen atoms N, the Zr–O distance, the Debye–Waller factor σ^2 and the energy threshold phase shift ΔE_0 were adjusted. The aim was to determine the coordination number and interatomic distances of Zr in Zr–AGuIX. Best-fit parameters are collected in Table 3 for Zr–A and Zr–AGuIX samples. Zr–A sample corresponds to a solution of Zr in HEPES and carbonate media (see Table 1) without AGuIX. It corresponds to the solution just before the addition of the nanoparticle and aims to confirm whether the nanoparticle influences the coordination mode of Zr.

For the Zr–A and Zr–AGuIX samples, best-fit results accurately reproduce the experimental EXAFS data (R-factor = 6 and 4%) and best-fit parameters are plausible. The best-fit results for Zr–AGuIX is shown in Fig. 6. Interestingly, both the coordination number and the fitted Zr–O distances decrease for Zr–AGuIX compared to Zr–A. It has been shown that when Zr is complexed with carbonate ions, the Zr–O bond is longer (2.21 Å) than when Zr is bound to hydroxyl groups (2.10 Å).[44] A decrease in the Zr–O bond length from 2.19 to 2.10 Å (upon adding AGuIX to the Zr solution containing carbonates) is consistent with the exchange of carbonate ligand with another ligand. Additionally, another study has shown that upon adding a carboxylic acid ligand to a solution with $[Zr(CO_3)_4]^{4-}$, a ligand exchange reaction was observed.[45] These findings confirm that the addition of the AGuIX nanoparticle to the Zr solution affects the coordination geometry of Zr. As the EXAFS part of the spectra cannot be investigated any further, the choice was made to study the XANES part.

XANES study

The XANES part of the XAS spectrum, spanning a region of 50–200 eV above the absorption edge, contains information about the local atomic and electronic structure around the absorbing atom. Previous studies on Zr have shown that its XANES threshold shape at the K-edge is highly dependent on its coordination number and symmetry.[46,47] To illustrate the differences which can be observed on the K-edge XANES spectra of Zr compounds, XANES spectra measured for three solid state compounds, baddeleyite (ZrO_2), zircon ($ZrSiO_4$) and perovskite ($ZrBaO_3$) are reproduced from the literature in Fig. 7. The XANES spectrum of baddeleyite (ZrO_2), has a rounded threshold shape with a single broad peak. For zircon ($ZrSiO_4$), the threshold is narrower, and the peak splits into two, with the first peak being more intense than the second. For the perovskite ($ZrBaO_3$), the peaks are more separated, with the second peak being more intense. These differences in XANES thresholds are attributed to differences in bond lengths and coordination numbers in the first coordination sphere of Zr. The rounded shape of the threshold is characteristic of a coordination number of 7 or 8 for zirconium and longer average Zr–O distances, such as baddeleyite (7 oxygen atoms at 2.166 Å),

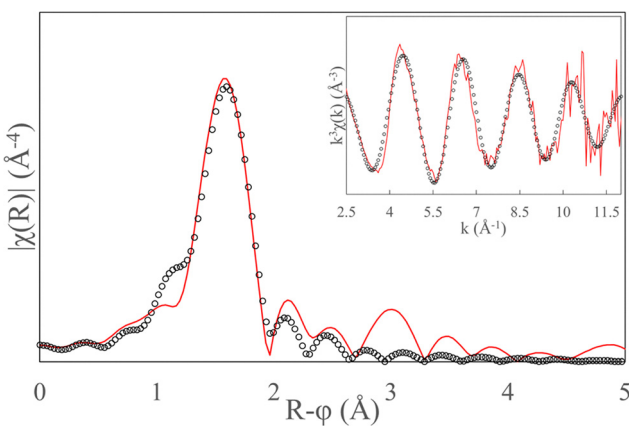

Fig. 6 Fourier transform of the Zr K-edge k^3-weighted EXAFS spectrum ($2.5 \leq k \leq 12$ Å^{-1}) of a Zr–AGuIX solution. Experimental data are in red lines and fit data in black circles. The data fitted using a one shell oxygen model over the range from 1 to 3 Å.

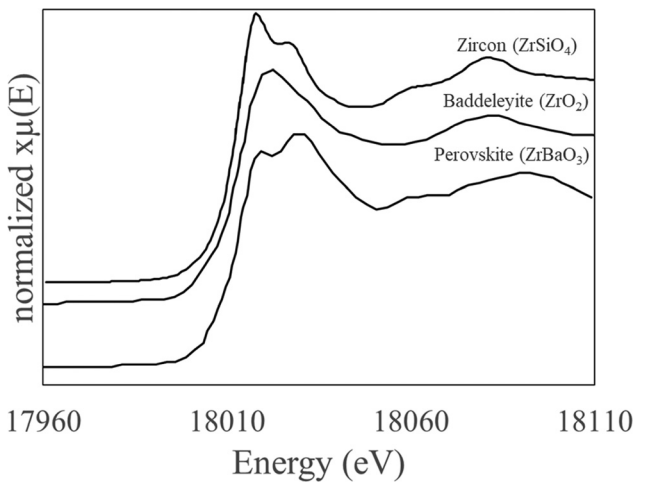

Fig. 7 K-edge XANES spectra of Zr of several zirconium reference compounds. The spectra have been traced using data from a previous study.[46]

zirconolite, $CaZrTi_2O_7$ (7 oxygen at 2.171 Å) and $Zr(SO_4)_2{\cdot}4H_2O$ (8 oxygen at 2.180 Å). The double peak of zircon (8 oxygens at an average distance of 2.198 Å), with the first peak more intense than the second, is characteristic of zirconium in an octahedral coordination site. For the perovskite, the presence of two peaks with the second one more intense than the first is due to weaker coordination around zirconium and shorter Zr–O distances (6 oxygen atoms at approximately 2.10 Å).

The XANES spectra of the Zr–DOTA and Zr–AGuIX samples are reproduced in Fig. 8. The threshold shape of the Zr–DOTA complex is highly similar to that of $ZrSiO_4$, with zirconium being bound to four nitrogen and four oxygen inside the cage resulting in a coordination of 8, like zircon. In contrast, the threshold shape of Zr–AGuIX more closely resembles that of perovskite, which has a coordination number of 6. The coordination number would be lower for Zr–AGuIX than for Zr–DOTA. This result is in agreement with the EXAFS fit, which indicated a lower coordination number for Zr–AGuIX. Furthermore, beyond the threshold (>18 050 eV), the first oscillation, which corresponds to the first wave in the EXAFS signal, occurs at higher energy for Zr–AGuIX than for Zr–DOTA, indicating shorter distances for Zr–AGuIX.

The XANES spectra of Zr–DOTA, Zr–DOTAGA, both synthesized with the same protocol (*via* an organic route), and Zr–AGuIX have been compared (see supporting information). The XANES spectrum of Zr–DOTAGA solution is very similar to the Zr–DOTA one. It seems that the chemical environment around Zr is similar in both structures. Moreover, as for Zr–DOTA, the XANES spectrum of Zr–DOTAGA is similar to that of zircon. The coordination number of Zr in the Zr–DOTAGA complex is therefore the same as for the Zr–DOTA complex (8). Thus, the supplementary arm of DOTAGA does not play a role in the complexation of Zr.

As for the EXAFS part, the XANES spectrum of Zr–AGuIX is compared with those of the Zr–A sample (Zr + carbonate in HEPES media before addition of the nanoparticle) and Zr–B solution (Zr + carbonate + DOTA in HEPES media). The spectra are shown in Fig. 8. Firstly, the XANES spectra of Zr–A and Zr–B samples are very similar, which is consistent with the EXAFS results shown previously. The XANES spectra of Zr–A sample and Zr–AGuIX solution (addition of NP AGuIX to the Zr–A solution) are very different, with a change in the absorption threshold maximum. The threshold of Zr–A is similar to that of baddeleyite indicating that Zr has a coordination number of 7 or 8. Moreover, Zr–A can correspond to a zirconium carbonate complex, such as ($Zr(CO_3)_4^{4-}$), in view of the synthesis medium. One study demonstrated that this monomeric species was predominant in solutions containing excess carbonate ($[(CO_3)^{2-}]/[Zr^{4+}] \geq 6$) at pH < 9.5,[44] with the carbonate ligands bidentate-bonded to Zr to form an 8-coordination complex.

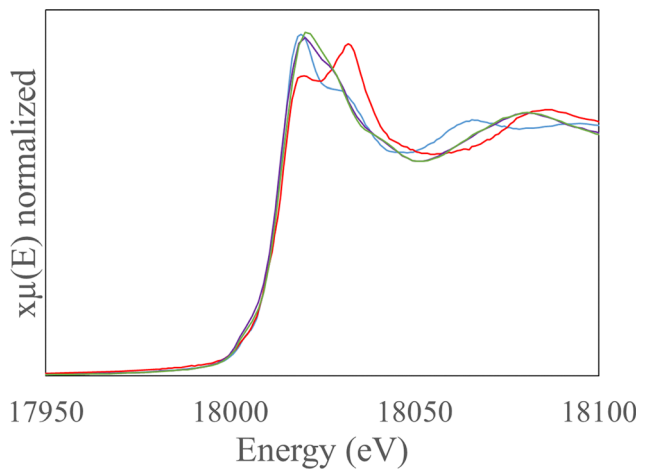

Fig. 8 K-edge XANES spectra of Zr–DOTA complex (blue), Zr–AGuIX solution (red), Zr–B sample (purple) and Zr–A sample (green).

In conclusion, the XANES results confirm the decrease in Zr coordination number when the AGuIX nanoparticle solution is added to the Zr–A solution. This shows that the coordination of 6 is due to the addition of the nanoparticle and not to other reagents in solution.

To better understand the effect of the ratio Zr : DOTA and the role of the carbonates in the coordination sphere of Zr, two additional samples were prepared and characterized. EXAFS and XANES spectra of Zr–AGuIX B (Zr : DOTA ratio of 1 : 6 instead of 1 : 2 in Zr–AGuIX sample) and Zr–AGuIX C (without carbonates) are presented in the supporting information. They are comparable to Zr–AGuIX sample. The Zr : DOTA ratio and the absence of carbonates appear to have little influence on the coordination mode of zirconium at the nanoparticle.

XANES simulation spectra

The XANES spectra have been simulated using FEFF code, which is largely used in the literature to simulate XANES spectra.[31,48,49] Thanks to the multiple scattering approach implemented in the code, previous studies have found that it is possible to reproduce correctly the XANES spectra of systems containing transition metals[50–55] and especially the K-edge of zirconium in the solid state and in solution.[55–57]

The previous results have demonstrated that the extra arm of DOTAGA compared with DOTA does not alter the Zr environment, and that Zr would be of coordinate 6 and not inside the DOTA cage in the Zr–AGuIX system. Tran *et al.* have proposed that Si–O^-, Si–OH and NH_2 groups are involved in Zr coordination. Silanol groups (Si–OH or Si–O^-) are the most likely to interact with zirconium. Previous studies have shown that silica nanoparticles without surface-grafted ligands can complex zirconium.[5,6,58] Chen *et al.* observed that deprotonated silanols played a key role in ^{89}Zr radiolabeling as a hard oxygen base to stabilize Zr(IV).[6] A literature search has been conducted to identify a crystallographic structure containing 6-fold zirconium bonded to Si–O^- groups that could be used as a model structure for simulating the XANES spectrum. Catapleiite ($Na_2Zr(Si_3O_9){\cdot}H_2O$) proved to be the ideal candidate.[59] This structure contains several zirconium atoms in 6-coordination and has Zr–O–Si bonds. The simulated K-edge spectrum of Zr from this structure is shown in Fig. 9. The shape and position of the simulated XANES spectrum is characteristic of Zr(IV) structures in alkalizirconosilicate systems (Na/Li/K, Si, Zr) such

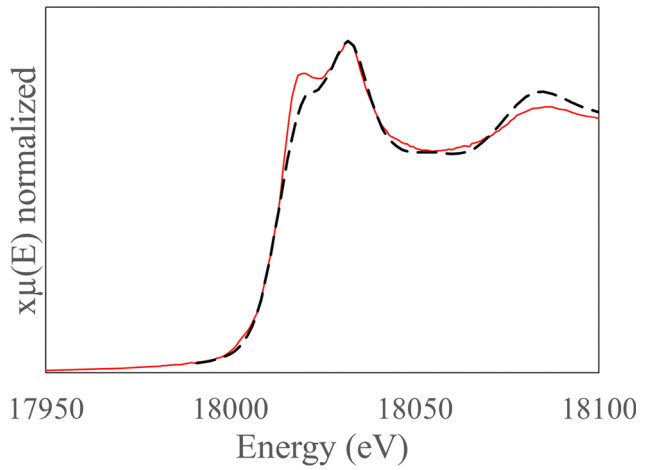

Fig. 9 K-edge XANES spectra of a Zr–AGuIX solution (red line) and simulated from the crystallographic structure of catapleiite (black dashed line). For normalization purposes, a multiplier of 1.07 has been applied to the simulated spectrum.

as vlasovite ($NaZrSi_6O_{15}$) or eudyalite ($Na_4(Ca, Ce, Fe, Mn, Y, La, Sr, K)_3ZrSi_8O_{22}(OH, Cl)_2$).[60–62] The simulated XANES spectrum of catapleiite reproduces the experimental spectrum of Zr AGuIX quite well (Fig. 9). This is consistent with a coordination number of 6 for Zr with silanol groups in the coordination sphere. However, the two spectra differ in the intensity of the first peak indicating that the first coordination sphere is not identical. Several hypotheses can explain this difference such as the presence of hydroxide, water or carbonate ligand in the coordination sphere of zirconium. Nevertheless, since Chen *et al.* observed that the complexation of Zr in unfunctionalized nanoparticles is weaker than in AGuIX (27% *vs.* 96%), this suggests that the ligand grafted onto the nanoparticle plays a role on the Zr–AGuIX interactions and that the carboxylate arms of free DOTAGA participate in the Zr coordination.

IV. Conclusion

This study has demonstrated the utility of X-ray absorption spectroscopy in characterizing the interaction between radiometal and hybrid silica-based nanoparticles which are developed in the context of nuclear medicine. ^{89}Zr is a particularly promising radioisotope, and its radiolabeling on the AGuIX nanoparticles is highly efficient. By combining EXAFS, XANES and theoretical calculation, we were able to obtain structural details on Zr complexation within the AGuIX nanoparticle. From previous work it was speculated that zirconium was complexed by DOTAGA and the presence of Si–O, Si–OH or NH_2 groups on the surface of the particle might facilitate the complexation of zirconium by DOTAGA by creating a microenvironment. The strategy applied in this work was to rule out the possible coordination mode one by one through EXAFS/XANES analysis in order to propose the coordination model most consistent with the experimental observations. EXAFS analysis shows that zirconium is not inserted into the DOTAGA cage in Zr–AGuIX despite what was originally expected. The XANES analysis also confirms that Zr in not within the DOTAGA tetraaza core, but that zirconium goes from a coordination of 8 to a coordination of 6 when it binds to the nanoparticle. The simulation of XANES spectra shows that deprotonated silanols are involved in the first coordination sphere of zirconium in Zr–AGuIX. If the tetraaza cavity is not involved in the binding, the strong carboxylate groups from free DOTAGA should complete the Zr coordination sphere and explain the high ^{89}Zr labelling yield of AGuIX compared to unfunctionalized silica nanoparticles.

These results indicate that flexible carboxylate functions may be sufficient to improve the zirconium radiolabeling efficiency on silica-based nanoparticles. Such information are important to improve radiolabeling strategies for nanoparticles.

Limitation of this work and applicability to reality

The purpose of this work was to provide a better understanding of the interactions between Zr and AGuIX nanoparticles. While clinical applications employ the radionuclide ^{89}Zr (at 10^{-7} mol L^{-1}), this study uses natural zirconium (at 7×10^{-4} mol L^{-1}), which introduces some limitations due to differing sources and experimental conditions. The main difference would be that, in radiolabeling conditions, no polymeric species is expected due to the very low concentrations. However, our experimental conditions similarly showed no evidence of zirconium clusters or polymeric species. Additionally, although radiolysis (radiation-induced degradation) does not occur in our system, a previous work has demonstrated that Zr–DOTA exhibit high resistance to radiolytic degradation and would therefore have minimal impact in the real system.[24]

This study did not involve any animal or human subjects. All experimental work was conducted in accordance with the relevant national and institutional guidelines of the University of Montpellier and in compliance with The French Charter of Ethics for Research Professions.

Conflicts of interest

The authors declare no conflict of interest.

Data availability

The data supporting this article have been included as part of the supplementary information (SI). Supplementary information is available. See https://doi.org/10.1039/d5cp04917b.

References

1 V. L. Tran, F. Lux and N. Tournier, *et al.*, Quantitative Tissue Pharmacokinetics and EPR Effect of AGuIX Nanoparticles: A Multimodal Imaging Study in an Orthotopic Glioblastoma Rat Model and Healthy Macaque, *Adv. Healthcare Mater.*, 2021, **10**(16), 2100656, DOI: 10.1002/adhm.202100656.
2 C. Truillet, E. Thomas, F. Lux, L. T. Huynh, O. Tillement and M. J. Evans, Synthesis and Characterization of 89 Zr-Labeled

Ultrasmall Nanoparticles, *Mol. Pharmaceutics*, 2016, **13**(7), 2596–2601, DOI: 10.1021/acs.molpharmaceut.6b00264.

3 T. M. Shaffer, S. Harmsen, E. Khwaja, M. F. Kircher, C. M. Drain and J. Grimm, Stable Radiolabeling of Sulfur-Functionalized Silica Nanoparticles with Copper-64, *Nano Lett.*, 2016, **16**(9), 5601–5604, DOI: 10.1021/acs.nanolett.6b02161.

4 D. Psimadas, P. Georgoulias, V. Valotassiou and G. Loudos, Molecular nanomedicine towards cancer: 111In-labeled nanoparticles, *J. Pharm. Sci.*, 2012, **101**(7), 2271–2280, DOI: 10.1002/jps.23146.

5 F. Chen, K. Ma and L. Zhang, *et al.*, Target-or-Clear Zirconium-89 Labeled Silica Nanoparticles for Enhanced Cancer-Directed Uptake in Melanoma: A Comparison of Radiolabeling Strategies, *Chem. Mater.*, 2017, **29**(19), 8269–8281, DOI: 10.1021/acs.chemmater.7b02567.

6 F. Chen, S. Goel and H. F. Valdovinos, *et al.*, In Vivo Integrity and Biological Fate of Chelator-Free Zirconium-89-Labeled Mesoporous Silica Nanoparticles, *ACS Nano*, 2015, **9**(8), 7950–7959, DOI: 10.1021/acsnano.5b00526.

7 A. B. Satterlee and L. Huang, Current and Future Theranostic Applications of the Lipid-Calcium-Phosphate Nanoparticle Platform, *Theranostics*, 2016, **6**(7), 918–929, DOI: 10.7150/thno.14689.

8 F. Silva, A. Paulo and A. Pallier, *et al.*, Dual Imaging Gold Nanoplatforms for Targeted Radiotheranostics, *Materials*, 2020, **13**(3), 513, DOI: 10.3390/ma13030513.

9 J. S. Choi, J. C. Park and H. Nah, *et al.*, A Hybrid Nanoparticle Probe for Dual-Modality Positron Emission Tomography and Magnetic Resonance Imaging, *Angew. Chem.*, 2008, **120**(33), 6355–6358, DOI: 10.1002/ange.200801369.

10 K. V. Katti, M. Khoobchandani and V. C. Thipe, *et al.*, Prostate tumor therapy advances in nuclear medicine: green nanotechnology toward the design of tumor specific radioactive gold nanoparticles, *J. Radioanal. Nucl. Chem.*, 2018, **318**(3), 1737–1747, DOI: 10.1007/s10967-018-6320-4.

11 M. Swierczewska, S. Lee and X. Chen, Inorganic Nanoparticles for Multimodal Molecular Imaging, *Mol. Imaging*, 2011, **10**(1), 00001, DOI: 10.2310/7290.2011.00001.

12 A. B. de Barros, A. Tsourkas, B. Saboury, V. N. Cardoso and A. Alavi, Emerging role of radiolabeled nanoparticles as an effective diagnostic technique, *EJNMMI Res.*, 2012, **2**(1), 39, DOI: 10.1186/2191-219X-2-39.

13 B. H. Hasegawa, K. Iwata and K. H. Wong, *et al.*, Dual-Modality Imaging of Function and Physiology, *Acad. Radiol.*, 2002, **9**(11), 1305–1321, DOI: 10.1016/S1076-6332(03)80564-0.

14 F. Lux, V. L. Tran and E. Thomas, *et al.*, AGuIX® from bench to bedside—Transfer of an ultrasmall theranostic gadolinium-based nanoparticle to clinical medicine, *BJR*, 2018, **92**(1093), 0365, DOI: 10.1259/bjr.20180365.

15 F. Lux, A. Mignot and P. Mowat, *et al.*, Ultrasmall Rigid Particles as Multimodal Probes for Medical Applications, *Angew. Chem., Int. Ed.*, 2011, **50**(51), 12299–12303, DOI: 10.1002/anie.201104104.

16 S. Bonvalot, C. Le Pechoux and T. De Baere, *et al.*, First-in-Human Study Testing a New Radioenhancer Using Nanoparticles (NBTXR3) Activated by Radiation Therapy in Patients with Locally Advanced Soft Tissue Sarcomas, *Clin. Cancer Res.*, 2017, **23**(4), 908–917, DOI: 10.1158/1078-0432.CCR-16-1297.

17 S. Bonvalot, P. L. Rutkowski and J. Thariat, *et al.*, NBTXR3, a first-in-class radioenhancer hafnium oxide nanoparticle, plus radiotherapy versus radiotherapy alone in patients with locally advanced soft-tissue sarcoma (Act.In.Sarc): a multicentre, phase 2–3, randomised, controlled trial, *Lancet Oncol.*, 2019, **20**(8), 1148–1159, DOI: 10.1016/S1470-2045(19)30326-2.

18 C. Chargari, P. Maury and M. Texier, *et al.*, Theragnostic Gadolinium-Based Nanoparticles Safely Augment X-ray Radiation Effects in Patients with Cervical Cancer, *ACS Nano*, 2024, **18**(26), 16516–16529, DOI: 10.1021/acsnano.3c12537.

19 A. Mignot, C. Truillet and F. Lux, *et al.*, A Top-Down Synthesis Route to Ultrasmall Multifunctional Gd-Based Silica Nanoparticles for Theranostic Applications, *Chem. – Eur. J.*, 2013, **19**(19), 6122–6136, DOI: 10.1002/chem.201203003.

20 F. S. Emami, V. Puddu and R. J. Berry, *et al.*, Force Field and a Surface Model Database for Silica to Simulate Interfacial Properties in Atomic Resolution, *Chem. Mater.*, 2014, **26**(8), 2647–2658, DOI: 10.1021/cm500365c.

21 S. V. Patwardhan, F. S. Emami and R. J. Berry, *et al.*, Chemistry of Aqueous Silica Nanoparticle Surfaces and the Mechanism of Selective Peptide Adsorption, *J. Am. Chem. Soc.*, 2012, **134**(14), 6244–6256, DOI: 10.1021/ja211307u.

22 D. N. Pandya, N. Bhatt and H. Yuan, *et al.*, Zirconium tetraazamacrocycle complexes display extraordinary stability and provide a new strategy for zirconium-89-based radiopharmaceutical development, *Chem. Sci.*, 2017, **8**(3), 2309–2314, DOI: 10.1039/C6SC04128K.

23 D. Parker, C. Pulukkody K, F. Smith, K. Batsanov A and J. A. Howard, Structures of the yttrium complexes of 1,4,7,10-tetraazacyclododecane- N, N′, N″, N‴-tetraacetic acid (H 4 dota) and N, N″-bis(benzylcarbamoylmethyl) diethylenetriamine-N, N′, N″-triacetic acid and the solution structure of a zirconium complex of H 4 dota, *J. Chem. Soc., Dalton Trans.*, 1994, **0**(5), 689–693, DOI: 10.1039/DT9940000689.

24 I. Mahti, D. Guillaumont, C. Berthon, G. Saint-Louis, X. Hérès and L. Berthon, Effect of metal complexation on the radiolytic stability of DOTA, *Dalton Trans.*, 2023, **52**(29), 9952–9963, DOI: 10.1039/D3DT00977G.

25 S. Finkeldei, M. Stennett and P. Kowalski, *et al.*, Insights into the fabrication and structure of plutonium pyrochlores, *J. Mater. Chem. A*, 2020, **8**, 2387–2403, DOI: 10.1039/C9TA05795A.

26 G. Chupin, C. Tamain, T. Dumas, P. L. Solari, P. Moisy and D. Guillaumont, Characterization of a Hexanuclear Plutonium(IV) Nanostructure in an Acetate Solution via Visible–Near Infrared Absorption Spectroscopy, Extended X-ray Absorption Fine Structure Spectroscopy, and Density Functional Theory, *Inorg. Chem.*, 2022, **61**(12), 4806–4817, DOI: 10.1021/acs.inorgchem.1c02876.

27 E. Acher, Y. Hacene Cherkaski and T. Dumas, *et al.*, Structures of Plutonium(IV) and Uranium(VI) with N,N-Dialkyl Amides from Crystallography, X-ray Absorption Spectra, and Theoretical Calculations, *Inorg. Chem.*, 2016, **55**(11), 5558–5569, DOI: 10.1021/acs.inorgchem.6b00592.

28 C. Truillet, E. Thomas, F. Lux, L. T. Huynh, O. Tillement and M. J. Evans, Synthesis and Characterization of 89 Zr-Labeled Ultrasmall Nanoparticles, *Mol. Pharmaceutics*, 2016, **13**(7), 2596–2601, DOI: 10.1021/acs.molpharmaceut.6b00264.

29 E. Thomas *Développement d'une seconde génération de nanoparticules AGuIX pour des applications théranostiques en oncologie*. These de doctorat. Université de Lyon; 2017. https://tel.archives-ouvertes.fr/tel-01674228.

30 N. E. Good, G. D. Winget, W. Winter, T. N. Connolly, S. Izawa and R. M. M. Singh, Hydrogen Ion Buffers for Biological Research, *Biochemistry*, 1966, **5**(2), 467–477, DOI: 10.1021/bi00866a011.

31 B. Ravel and M. Newville, *ATHENA*, *ARTEMIS*, *HEPHAESTUS*: data analysis for X-ray absorption spectroscopy using *IFEFFIT*, *J. Synchrotron Rad.*, 2005, **12**(4), 537–541, DOI: 10.1107/S0909049505012719.

32 A. J. Connelly, N. C. Hyatt, K. P. Travis, R. J. Hand, E. R. Maddrell and R. J. Short, The structural role of Zr within alkali borosilicate glasses for nuclear waste immobilisation, *J. Non-Cryst. Solids*, 2011, **357**(7), 1647–1656, DOI: 10.1016/j.jnoncrysol.2011.01.005.

33 M. J. Frisch, G. W. Trucks, H. B. Schlegel, *et al.* Gaussian 16. Gaussian, Inc. Wallingford, CT; 2016.

34 C. Adamo and V. Barone, Toward reliable density functional methods without adjustable parameters: The PBE0 model, *J. Chem. Phys.*, 1999, **110**(13), 6158–6170, DOI: 10.1063/1.478522.

35 D. Andrae, U. Häußermann, M. Dolg, H. Stoll and H. Preuß, Energy-adjustedab initio pseudopotentials for the second and third row transition elements, *Theor. Chim. Acta*, 1990, **77**(2), 123–141, DOI: 10.1007/BF01114537.

36 J. Tomasi, B. Mennucci and R. Cammi, Quantum Mechanical Continuum Solvation Models, *Chem. Rev.*, 2005, **105**(8), 2999–3094, DOI: 10.1021/cr9904009.

37 J. J. Rehr, J. J. Kas, F. D. Vila, M. P. Prange and K. Jorissen, Parameter-free calculations of X-ray spectra with FEFF9, *Phys. Chem. Chem. Phys.*, 2010, **12**(21), 5503–5513, DOI: 10.1039/B926434E.

38 M. Alex Brown, T. Brossard and D. A. Rotsch, Examination of lutetium(III)-DOTA and copper(II)-NOTA solution structures using EXAFS, *Inorg. Chim. Acta*, 2018, **482**, 118–121, DOI: 10.1016/j.ica.2018.05.031.

39 J. Moreau, E. Guillon, J. C. Pierrard, J. Rimbault, M. Port and M. Aplincourt, Complexing Mechanism of the Lanthanide Cations Eu3 +, Gd3 +, and Tb3+ with 1,4,7,10-Tetrakis(carboxymethyl)-1,4,7,10-tetraazacyclododecane (dota)—Characterization of Three Successive Complexing Phases: Study of the Thermodynamic and Structural Properties of the Complexes by Potentiometry, Luminescence Spectroscopy, and EXAFS, *Chem. – Eur. J.*, 2004, **10**(20), 5218–5232, DOI: 10.1002/chem.200400006.

40 S. L. Wu and W. D. Horrocks Jr, Kinetics of Complex Formation by Macrocyclic Polyaza Polycarboxylate Ligands: Detection and Characterization of an Intermediate in the Eu3+ -dota System by Laser-Excited Luminescence, *Inorg. Chem.*, 1995, **34**(14), 3724–3732, DOI: 10.1021/ic00118a020.

41 M. Audras, L. Berthon and C. Berthon, *et al.*, Structural Characterization of Am(III)- and Pu(III)-DOTA Complexes, *Inorg. Chem.*, 2017, **56**(20), 12248–12259, DOI: 10.1021/acs.inorgchem.7b01666.

42 C. Hennig, S. Weiss, W. Kraus, J. Kretzschmar and A. C. Scheinost, Solution Species and Crystal Structure of Zr(IV) Acetate, *Inorg. Chem.*, 2017, **56**(5), 2473–2480, DOI: 10.1021/acs.inorgchem.6b01624.

43 C. Tamain, T. Dumas, C. Hennig and P. Guilbaud, Coordination of Tetravalent Actinides (An = Th^{IV}, U^{IV}, Np^{IV}, Pu^{IV}) with DOTA: From Dimers to Hexamers, *Chem. – Eur. J.*, 2017, **23**(28), 6864–6875, DOI: 10.1002/chem.201700493.

44 F. Takasaki, K. Fujiwara and Y. Nakajima, *et al.*, A monomeric [Zr(CO3)4]4− complex in an ammonium zirconium carbonate aqueous solution studied by extended X-ray absorption fine structure, Raman and nuclear magnetic resonance spectroscopy, *Dalton Trans.*, 2014, **44**(2), 645–652, DOI: 10.1039/C4DT02022G.

45 F. Takasaki, K. Fujiwara and T. Kikuchi, *et al.*, Ligand Exchange Reactions of a Monomeric Zirconium Carbonate Complex with Carboxylic Acids Studied by Extended X-ray Absorption Fine Structure, UV Absorption and Raman Spectrophotometry, *Anal. Sci.*, 2017, **33**, 1007–1012, DOI: 10.2116/analsci.33.1007.

46 R. B. Greegor, K. Y. Blohowiak, J. H. Osborne, K. A. Krienke, J. T. Cherian and F. W. Lytle, X-Ray Spectroscopic Investigation of the Zr-Site in Thin Film Sol-Gel Surface Preparations, *J. Sol-Gel Sci. Technol.*, 2001, **20**(1), 35–50, DOI: 10.1023/A:1008772532638.

47 A. J. Connelly, N. C. Hyatt, K. P. Travis, R. J. Hand, E. R. Maddrell and R. J. Short, The structural role of Zr within alkali borosilicate glasses for nuclear waste immobilisation, *J. Non-Cryst. Solids*, 2011, **357**(7), 1647–1656, DOI: 10.1016/j.jnoncrysol.2011.01.005.

48 E. Bosman and J. Thieme, Modeling of XANES-spectra with the FEFF-program, *J. Phys.: Conf. Ser.*, 2009, **186**(1), 012004, DOI: 10.1088/1742-6596/186/1/012004.

49 K. Nakanishi and T. Ohta, Verification of the FEFF simulations to K-edge XANES spectra of the third row elements, *J. Phys.:Condens. Matter*, 2009, **21**(10), 104214, DOI: 10.1088/0953-8984/21/10/104214.

50 C. S. Spanjers, P. Guillo, T. D. Tilley, M. J. Janik and R. M. Rioux, Identification of Second Shell Coordination in Transition Metal Species Using Theoretical XANES: Example of Ti–O–(C, Si, Ge) Complexes, *J. Phys. Chem. A*, 2017, **121**(1), 162–167, DOI: 10.1021/acs.jpca.6b12197.

51 P. Liebisch, M. Haumann and H. Dau, Simulation of XANES spectra for protein-bound metal centers: analysis of linear dichroism data, *Phys. Scr.*, 2005, **2005**(T115), 859, DOI: 10.1238/Physica.Topical.115a00859.

52 G. A. Waychunas, C. C. Fuller, J. A. Davis and J. J. Rehr, Surface complexation and precipitate geometry for aqueous

Zn(II) sorption on ferrihydrite: II. XANES analysis and simulation, *Geochim. Cosmochim. Acta*, 2003, **67**(5), 1031–1043, DOI: 10.1016/S0016-7037(02)01280-2.

53 F. Farges, G. E. Brown and J. J. Rehr, Ti K-edge XANES studies of Ti coordination and disorder in oxide compounds: Comparison between theory and experiment, *Phys. Rev. B:Condens. Matter Mater. Phys.*, 1997, **56**(4), 1809–1819, DOI: 10.1103/PhysRevB.56.1809.

54 Y. Izumi, F. Kiyotaki and H. Yoshitake, *et al.*, Structure of low concentrations of vanadium on TiO 2 determined by XANES and ab initio calculations, *Chem. Commun.*, 2002, 2402–2403, DOI: 10.1039/B207159B.

55 D. Y. Cho, X-ray Absorption Spectroscopy and Its Simulation for Some Disordered Oxide Systems, *IOP Conf. Ser: Mater. Sci. Eng.*, 2020, **835**(1), 012003, DOI: 10.1088/1757-899X/835/1/012003.

56 M. Wilke, C. Schmidt and J. Dubrail, *et al.*, Zircon solubility and zirconium complexation in H2O + Na2O + SiO2 ± Al2O3 fluids at high pressure and temperature, *Earth Planet. Sci. Lett.*, 2012, **349–350**, 15–25, DOI: 10.1016/j.epsl.2012.06.054.

57 S. Jahn, J. Dubrail and M. Wilke, Complexation of Zr and Hf monomers in supercritical aqueous solutions: Insights from ab initio molecular dynamics simulations, *Chem. Geol.*, 2015, **418**, 30–39, DOI: 10.1016/j.chemgeo.2014.10.012.

58 T. M. Shaffer, M. A. Wall and S. Harmsen, *et al.*, Silica Nanoparticles as Substrates for Chelator-free Labeling of Oxophilic Radioisotopes, *Nano Lett.*, 2015, **15**(2), 864–868, DOI: 10.1021/nl503522y.

59 G. D. Ilyushin, A. A. Voronkov, V. V. Ilyukhin, N. N. Nevskii and N. V. Belov Crystal structure of natural monoclinic catapleiite Na2ZrSi3O9·2H2O, *Soviet Physics Doklady*, 1981, vol. 26, p. 808.

60 M. Louvel, C. Sanchez-Valle, W. J. Malfait, D. Testemale and J. L. Hazemann, Zr complexation in high pressure fluids and silicate melts and implications for the mobilization of HFSE in subduction zones, *Geochim. Cosmochim. Acta*, 2013, **104**, 281–299, DOI: 10.1016/j.gca.2012.11.001.

61 P. J. Dunn, R. C. Rouse, B. Cannon and J. A. Nelen, Zektzerite; a new lithium sodium zirconium silicate related to tuhualite and the osumilite group, *Am. Mineral.*, 1977, **62**(5–6), 416–420.

62 L. Horváth, R. A. Gault and J. Van Velthuizen *The Mineralogy of Mont Saint-Hilaire, Quebec*, Mineralogical Record; 1990.